ACS OMEGA

http://pubs.acs.org/journal/acsodf

Article

Fabricating Heterostructures for Boosting the Structure Stability of Li-Rich Cathodes

Yao Li, Qing Zhao, Mengke Zhang, Lang Qiu, Zhuo Zheng, Yang Liu, Yan Sun, Benhe Zhong, Yang Song,* and Xiaodong Guo

Cite This: *ACS Omega* 2023, 8, 6720−6728

Read Online

ACCESS | Metrics & More | Article Recommendations | Supporting Information

ABSTRACT: Li-rich Mn-based oxides are regarded as the most promising new-generation cathode materials, but their practical application is greatly hindered by structure collapse and capacity degradation. Herein, a rock salt phase is epitaxially constructed on the surface of Li-rich Mn-based cathodes through Mo doping to improve their structural stability. The heterogeneous structure composed of a rock salt phase and layered phase is induced by Mo^{6+} enriched on the particle surface, and the strong Mo−O bonding can enhance the TM−O covalence. Therefore, it can stabilize lattice oxygen and inhibit the side reaction of the interface and structural phase transition. The discharge capacity of 2% Mo-doped samples (Mo 2%) displays 279.67 mA h g^{-1} at 0.1 C (vs 254.39 mA h g^{-1} (pristine)), and the discharge capacity retention rate of Mo 2% is 79.4% after 300 cycles at 5 C (vs 47.6% (pristine)).

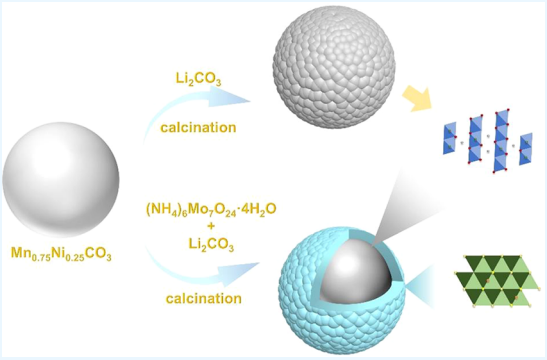

INTRODUCTION

Li-rich Mn-based cathode materials have great advantages over other cathode materials due to their high operating voltage and high energy density.[1−8] The high capacity is mainly provided by the cation redox reaction and anion redox reaction.[9−12] At 2−4.45 V, the transition metal ions undergo reversible redox processes (Ni^{2+}/Ni^{4+} and Co^{3+}/Co^{4+}) which are the cation redox reaction.[13−16] This process is often accompanied by transition metal migration, thus inducing phase transition.[17−22] At 4.45−4.8 V, lattice O undergoes a redox reaction to provide charge compensation, which is the anion redox reaction.[23−25] With irreversible O_2 loss, it leads to structure collapse, capacity degradation, and poor cycling performance.[16,26,27] The severe challenge of structural attenuation and capacity degradation in the electrochemical cycle also seriously hinders their practical application.[4]

Researchers have done a lot to address the above problems, such as surface coating[28−33] and doping.[34−37] Surface coating layers can effectively isolate electrolytes from the cathode surface and inhibit side reactions and HF corrosion, thus suppressing phase transition,[29] but there is an interface gap between the surface coating layer and particle, which also increases the Li^+ transmission resistance. Furthermore, it is unable to stabilize the O in a crystal lattice effectually.[38] On the contrary, ionic doping can change the O network and Li^+ diffusion route, which stabilizes the lattice O and enhances the rate performance of Li-rich Mn-based cathode materials.[39] However, the surface cannot be protected from side reactions. Moreover, we find that the rock salt phase is electrochemically inert and possesses a high reaction energy barrier with the electrolyte and thus can effectively inhibit side reactions.[40] The electrochemical performance of materials can be partly improved by the above modification measures. Considering comprehensively, we try to regulate the lattice and surface of materials at the same time, that is, to achieve the stability of lattice O and surface protection while avoiding the gap transmission resistance of the coating layer. For this purpose, we use Mo doping to situ induce the formation of heterostructures combined with a layered phase and rock salt on the surface. The surface-enriched Mo^{6+} converts part of Ni^{3+} into Ni^{2+} due to the charge conservation, and the increased Ni^{2+} occupies the Li site, thus forming a rock salt phase as a protective layer.[41]

For this subject, we chose $(NH_4)_6Mo_7O_{24}\cdot 4H_2O$ as the molybdenum source, calcined at 850 °C to realize Mo doping and construct a composite structure of a layered phase and rock salt phase on the surface in situ. Due to the charge conservation, the formation of the rock salt phase can be induced by Mo^{6+}.[41] Besides, a strong Mo−O bond can enhance the TM−O covalence and stabilize the O in the crystal lattice.[39] Compared with the pristine (PLLR), the

Received: November 16, 2022
Accepted: February 2, 2023
Published: February 13, 2023

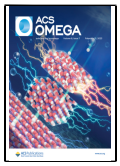

https://doi.org/10.1021/acsomega.2c07313
ACS Omega 2023, 8, 6720−6728

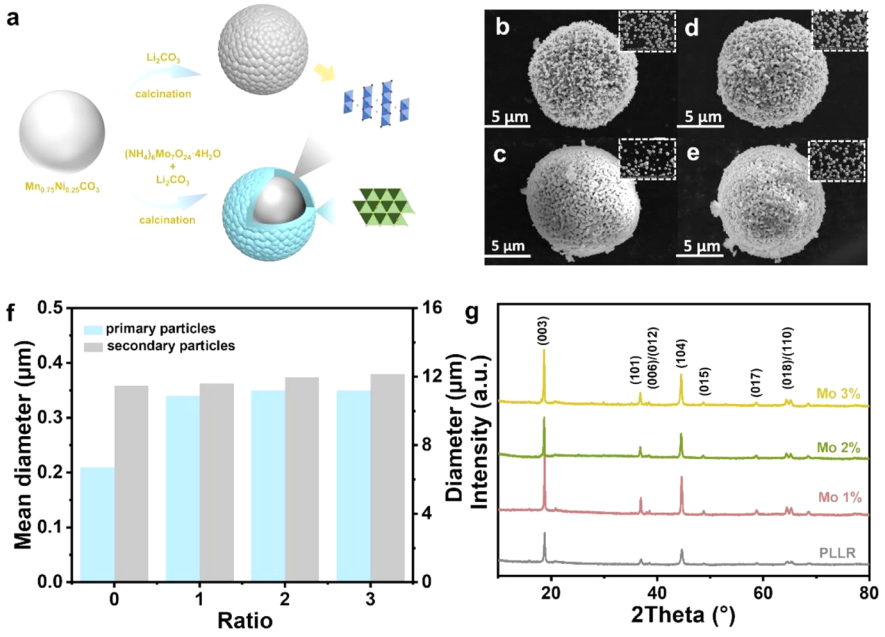

Figure 1. (a) Experimental flowchart of Mo^{6+} doping. (b) SEM images of pristine. (c) Mo 1%, (d) Mo 2%, and (e) Mo 3% at different magnifications. (f) Statistical diagram of particle size. (g) X-ray patterns of all samples.

electrochemical performances of the modified samples are greatly improved, particularly for the Mo 2% sample. This work provides a new idea for consolidating the structure stability of Li-rich materials.

EXPERIMENTAL SECTION

Materials Preparation. The precursor ($Mn_{0.75}Ni_{0.25}CO_3$) is prepared by the carbonate coprecipitation method. The mixed solution of 2 M $NiSO_4\cdot 6H_2O$ and $MnSO_4\cdot H_2O$ (Ni/Mn molar ratio is 1:3), 2 M Na_2CO_3 (precipitant), and 0.2 M $NH_3\cdot H_2O$ (chelating agent) are added into a 500 mL continuous stirred tank reactor through three peristaltic pumps. During the coprecipitation process, the pH is always kept at 8.0; the temperature is maintained at 50 °C; and the carbonate precursor is obtained after continuous stirring for 8 h, filtration with pure water, washing, and drying in an oven at 120 °C for 12 h.

For the preparation of the original sample ($Li_{1.2}Mn_{0.6}Ni_{0.2}CO_3$), the precursor is ground and mixed with an excess of 5% Li_2CO_3 in a mortar, and the mixture is put in a tubular furnace and calcined at 500 °C for 5 h at a heating rate of 5 °C min^{-1} and then calcined at 850 °C for 12 h. Then the mixture is cooled naturally to room temperature (25 °C).

For the preparation of the modified sample, the precursor is ground, and the precursor and ammonium molybdate are mixed in different molar proportions (1%, 2%, and 3%) with an excess of 5% Li_2CO_3 in a mortar. The the mixture is put in a tubular furnace and calcined at 500 °C for 5 h at a heating rate of 5 °C min^{-1} and then calcined at 850 °C for 12 h. The the mixture is cool naturally to room temperature. Corresponding to doping content, the modified sample is referred to as Mo x% (x = 1, 2, and 3).

Physical Characterization. The details of the materials' crystal structures are tested by powder X-ray diffraction (XRD), at a scan speed of 0.03367° s^{-1} with Cu Kα radiation. The Fullprof software is used to perform the Refine treatment. The surface composition and elemental valence state are obtained by X-ray photoelectron spectroscopy (XPS, Al Kα radiation) and calibrated by C 1s (284.8 mV). and in situ XPS is obtained to observe the change of O 1s during the first cycle of charging and discharging. The XPS Peak-Fit software is used to fit spectrum data. The morphology of all materials is evaluated by scanning electron microscopy (SEM). High-resolution transmission electron microscopy (HRTEM) with FEI Talos F200x is used to explore the selected area electron diffraction (SAED) patterns and elemental distribution mapping (EDS mapping). The Digital-Micrograph software is used for obtaining the Fourier transform (FFT) images.

Electrochemical Measurements. The electrochemical test is conducted in a CR2025 coin cell battery. The cathode material of CR2025, the coin cell battery is: 80% active material, 10% conductive agent (acetylene black), 10% poly(vinylidene fluoride) adhesive (PVDF), and *n*-methyl-2-pyrrolidine (NMP) as the solvent. It is mixed and ground and then evenly coated on an aluminum foil surface, dried at 120 °C for 12 h in a vacuum, and cut it into a circular electrode with a 10 mm diameter. The battery assembly process is completed in a glovebox filled with Ar. The cathode material of the battery is lithium metal, and the PP diaphragm is used as a separator and pressed under the pressure of 0.65 kPa with electrolytes. The electrochemical test is finished at 25 °C at 2.0−4.8 V through the Sunway channel. Electrochemical impedance spectroscopy (EIS) is obtained on the Zennium IM6 workstation at 2.0−4.8 V and a frequency range from 100 kHz to 10 mHz. For galvanostatic intermittent titration technique measurement (GITT), we discharge/charge the battery with a constant current for 10 min and then place it on the open-circuit table for 1 h.

RESULTS AND DISCUSSION

Mo doping and heterostructure construction are realized after sintering (Figure 1a). All samples show a typical spherical porous secondary particle composed of uniform and dense

https://doi.org/10.1021/acsomega.2c07313
ACS Omega 2023, 8, 6720−6728

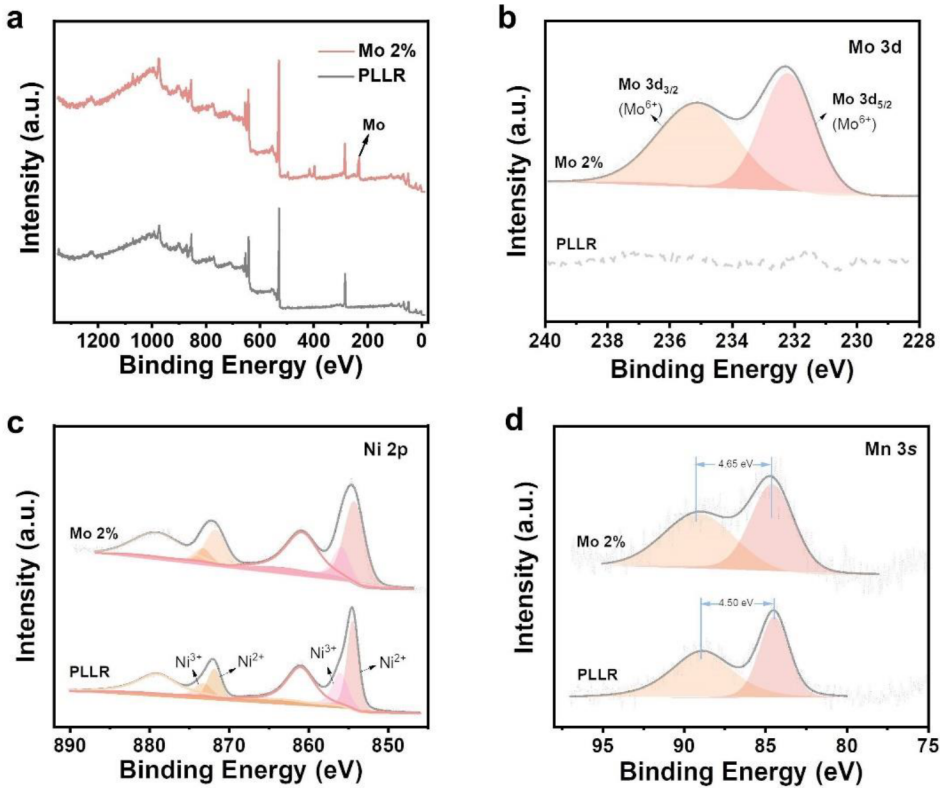

Figure 2. X-ray photoelectron spectroscopy (XPS) of different elements in PLLR and Mo 2%. (a) Full spectrum of XPS. (b) Mo 3d, (c) Ni 2p, and (d) Mn 3s.

primary particles (Figure 1b–e). The secondary particles of PLLR, Mo 1%, Mo 2%, and Mo 3% have similar diameters and display particle sizes of 11.48, 11.61, 11.97, and 12.16 μm, respectively, but the primary particles become bigger after modification (Figure 1f). Mo^{6+} doping can decrease the surface formation energy of the primary particles and increase their particle size, thereby changing the particle morphology.[42] EDS mapping images (Figure S1) further show that Mo can be uniformly distributed.

The crystal structures of the PLLR, Mo 1%, Mo 2%, and Mo 3% are explored by powder X-ray diffraction (XRD) (Figure 1g). All samples have characteristic diffraction peaks corresponding to the $R\bar{3}m$ space group of the α-$NaFeO_2$ structure. In addition, typical characteristic peaks of the Li_2MnO_3 phase ($C2/m$ structure group) are shown between 20° and 25°.[43] The clear splits of the (006)/(102) and (108)/(110) peaks mean all samples show a well-layered crystal structure, indicating that Mo doping does not damage the structure of the material.[44] The (003) peak offsets to a low angle after modification, indicating that Mo^{6+} is successfully doped into the particles.[45] As shown in Figure S2a–d and Table S1, the lattice parameters are analyzed by the Rietveld refinement method. With the increase of doping amount, both c and v increase in varying degrees. This is because the radius of Mo^{6+} (0.59 Å), which is bigger than $Ni^{3+}$and Mn^{4+} (0.56 and 0.53 Å), makes the layer space enlarged. Besides, part of Ni^{3+} (0.56 Å) is turned into larger Ni^{2+} (0.69 Å) due to the charge conservation.[46] However, when Mo doping is excessive, c shrinks a little due to the strong Mo–O bond energy. $I(003)/I(104)$ before and after modification is greater than 1.2, suggesting that all samples have a well-order layered structure.[3]

Moreover, we study the surface composition and elemental valence state of the samples before and after modification by X-ray photoelectron spectroscopy (XPS). In the full XPS spectrum, the characteristic peak of Mo 3d can be seen clearly, proving the existence of Mo (Figure 2a). In the Mo 3d spectrum, the characteristic peaks of Mo $3d_{5/2}$ (235 eV) and Mo $3d_{3/2}$ (232 eV) exist, which can prove the valence state of Mo in the particles (Mo^{6+}).[41] For the Ni 2p spectra of PLLR and Mo 2%, both Ni^{2+} (854.4 eV) and Ni^{3+} (856.0 eV) can be observed in Ni $2p_{3/2}$, and the relative intensity of the Ni^{2+} peak increases from 65.9% to 75.3% after modification, indicating that the content of Ni^{2+} increases.[47,48] The radius of Ni^{2+} is similar to that of Li^+, making it more inclined to occupy the Li site, thus forming a rock salt phase as a protective layer, protecting the crystal structure and inhibiting phase transition.[49] It can be known that the ΔE_{3s} of PLLR and Mo 2% are similar, at 4.50 and 4.65 eV, respectively (Figure 2d). In addition, Mn 3s ΔE_{3s} and the valence states of Mn have the following linear relationship:[3,50]

$$v_{Mn} = 9.67 - 1.27\Delta E_{3s}$$

According to this formula, the valence states of Mn in the PLLR and Mo 2% are +3.96 and +3.76, respectively. It is speculated that the valence state change of Mn is related to the charge compensation caused by Mo^{6+} doping because the low oxidation valence state of Mn supports its further oxidation and provides capacity.[46] In the O 1s spectrum (Figure S3a), the characteristic peak at 529.5 eV represents oxygen in the form of lattice oxygen (TM–O), and the characteristic peak at 532.1 eV represents weak carbonate species on the surface (CO_3^{2-}).[51,52] The analysis results show that the proportion of lattice oxygen increases slightly after modification (66.2% →

https://doi.org/10.1021/acsomega.2c07313
ACS Omega 2023, 8, 6720–6728

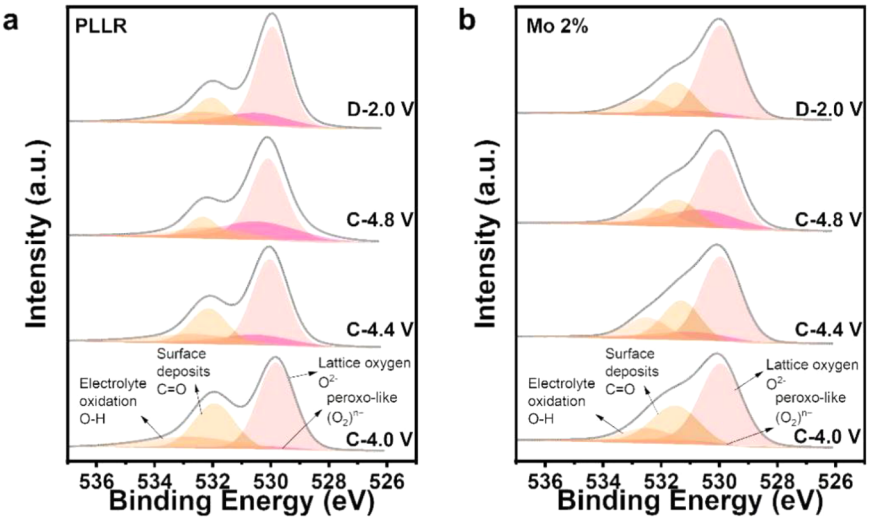

Figure 3. In situ XPS of O 1s measured at C-4.0, 4.4, and 4.8 V and D-2.0 V for (a) PLLR and (b) Mo 2%.

66.8%), reducing residual Li on the surface. In addition, the chemical characteristics of the outer surface area of the PLLR sample and Mo 2% particles are further investigated by XPS within the etching depth of 60 nm (0.33 nm/s), as shown in Figure S3b−h. The results show that the concentrations of all elements hardly changed near the particle surface, except Mo. However, the concentration of Mo distributes a gradient trend, which decreases from outside to inside, indicating that Mo^{6+} enters the material and is enriched on the surface after calcination. The quantitative analysis results (Table S2) show that the Mo content gradually decreases with the depth. At the same time, the peak value of Mo^{6+} does not shift significantly with the deepening of the etching depth, indicating that the valence state of Mo does not change with the change of etching depth. Combined with XRD analysis, it can be inferred that as the concentration of Mo^{6+} decreases with depth more Mo^{6+} near the surface leads to the increase of Ni^{2+} and the aggravation of cation mixing. Some Ni^{2+} migrates from the transition metal layer to the Li layer, resulting in the formation of the rock salt phase near the surface.[49]

To study the effect of Mo doping on the redox reaction of lattice oxygen, in situ XPS was carried out on the O 1s region of the PLLR and Mo 2% when charging to 4.0, 4.4, and 4.8 V and then discharging to 2.0 V during the first cycle (Figure 3). During charging to 4.8 V, the anion redox reaction results in the oxidation of the lattice oxygen (O^{2-}) to form peroxo-like oxygen ($(O_2)^{n-}$). Therefore, the intensity of the characteristic peaks of peroxo-like oxygen (530.7 eV) in both samples increases significantly, and the intensity of the characteristic peaks of lattice oxygen (529.8 eV) decreases. When discharging to 2 V, the intensity of the characteristic peaks of peroxo-like oxygen decreases with various degrees. It was found that the characteristic peaks of peroxides in the modified sample basically disappeared, and the lattice oxygen peak increased compared with the PLLR sample, indicating that the anion redox reaction in the Mo 2% sample was more reversible.[53,54]

TEM analyses are carried out to study the surface microstructure, and it can be observed that the microstructure near the particle surface of PLLR is a complete and uniform layered structure (Figure 4a). The local HRTEM images and the corresponding FFT diagrams can confirm that, with point

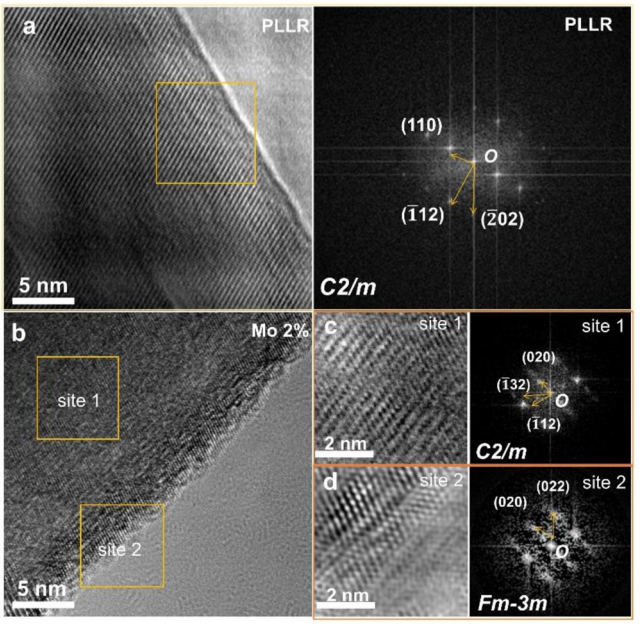

Figure 4. Sample HRTEM images before the cycles: (a) PLLR and (b−d) Mo 2%.

O as the starting point of the vector, three planes are (110), (−112), and (−202) planes of the $C2/m$ phase structure, respectively. The analysis of Mo 2% shows that the material structure is mainly divided into two areas, site 1 and site 2, which correspond to the $C2/m$ phase and $Fm\bar{3}m$ phase, respectively (Figure 4b−d). The formation of the rock salt phase on the surface is mainly attributed to the doping of some Mo^{6+}, which leads to the migration of some Ni^{2+} from the TM layer to the Li layer.[49] The epitaxial rock salt phase growth is helpful to maintain the surface and structure stability. Combined with the above XPS and XRD analyses, it can be concluded that Mo doping can construct a rock salt phase on the surface.

The electrochemical properties of all samples are characterized, as shown in Figure 5. The specific discharge capacities (0.1 C) of PLLR, Mo 1%, Mo 2%, and Mo 3% are 254.39, 277.27, 279.67, and 268.75 mA h g^{-1} corresponding to their

https://doi.org/10.1021/acsomega.2c07313
ACS Omega 2023, 8, 6720−6728

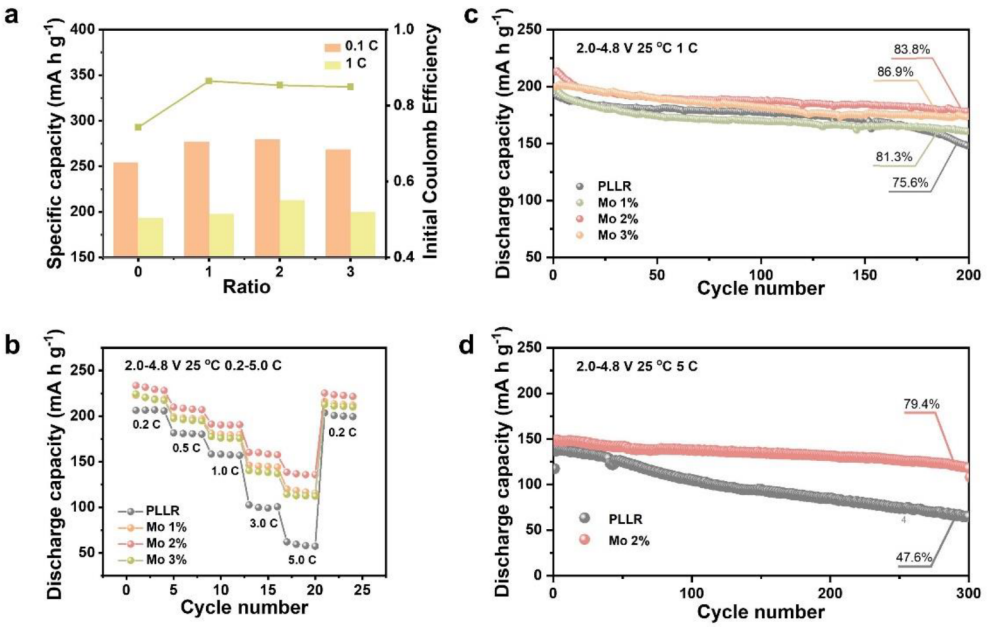

Figure 5. (a) First-Coulomb efficiency and first cycle discharge capacity at 0.1 and 1 C of all samples. (b) The discharge capacity of all samples at different rates (0.2 C, 0.5 C, 1 C, 3 C, 5 C). The cycling performance at (c) 1 C and (d) 5 C.

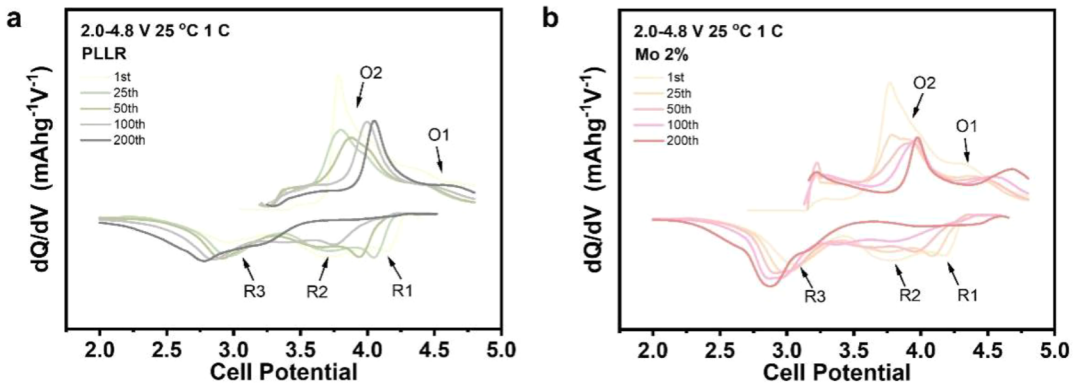

Figure 6. dQ/dV curves of (a) the PLLR and (b) Mo 2%.

first-Coulomb efficiencies of 74.3%, 86.5%, 85.4%, and 84.9% and the specific discharge capacities of 1 C of 193.59, 197.69, 212.98, and 199.85 mA h g^{-1}, respectively. In addition, as for the rate performance, the improved electrodes show better ability than the PLLR electrode at different rates. At 5 C, the discharge capacity of the Mo 2% sample reaches 138.60 mA h g^{-1}, much higher than the original 62.17 mA h g^{-1} (Figure 5b). Besides, the cycle performance of the modified samples is also improved. After 200 cycles at 1 C, the capacity is 148.23, 160.82, 178.39, and 173.73 mA h g^{-1} with a capacity retention of 75.6%, 81.3%, 83.8%, and 86.9%, respectively (Figure 5c). The PLLR and Mo 2% electrodes are cycled for 300 cycles at 5 C, and the Mo 2% sample still has a specific discharge capacity of 118.03 mA h g^{-1} and a capacity retention rate of 79.4%, which is much better than 65.33 mA h g^{-1} and 47.6% of the PLLR (Figure 5d). Comparing the discharge curves of PLLR and Mo 2% samples at the 1st, 25th, 50th, 100th, and 200th cycles, it can be found that the voltage attenuation is suppressed after Mo doping (Figure S4). The above results show that this modification measure improves the electrochemical performance effectively, and the cycle stability of Mo 2% is optimal. It also further proves that a rock salt phase can be epitaxially constructed on the surface by Mo doping. The formation of heterostructures can effectively slow down the reaction of electrolyte, inhibit HF attack, stabilize lattice O, and improve material structure stability.[36,41] Subsequent impedance calculations further support this view (Figure 6). The first charging process of the material contains two oxidation reactions: (1) Li^+ is extracted from the $LiMO_2$ component ($R\bar{3}m$ phase) at 4.0 V (O2), and a Ni^{2+}/Ni^{4+} oxidation reaction occurs. (2) Partially irreversible Li^+, at 4.5 V (O1), O^{2-}/O_2^{n-} ($1 < n < 3$), is extracted from the Li_2MnO_3 component ($C2/m$ phase) through the anion oxidation reaction of O_2. The corresponding peaks of O1 and O2 are reduction reactions of R1 (4.3 V) and R2 (3.7 V), respectively. The R3 peak is related to the Mn^{4+}/Mn^{3+} reaction at 3.4 V.[7] Mo 2% shows a larger R3 peak than PLLR, representing more reduction reactions and discharge capacity, and the degradation and polarization of the battery potential of Mo-doped samples during the cycle do not significantly decrease, which is speculated to be related to the increase of Ni^{2+} leading to the intensification of cation mixing.

The EIS diagrams (Figure S5) are composed of two semicircles. The high-frequency semicircle reflects the surface

https://doi.org/10.1021/acsomega.2c07313
ACS Omega 2023, 8, 6720−6728

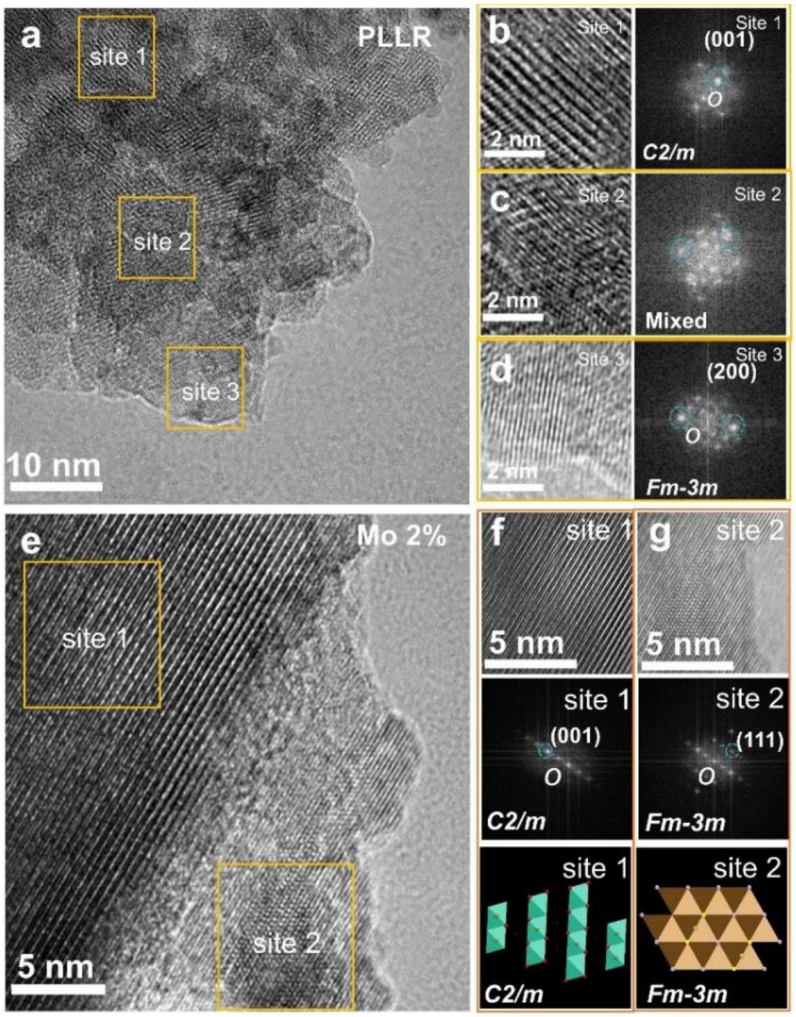

Figure 7. Sample HRTEM images after the cycles: (a–d) PLLR and (e–g) Mo 2%.

SEI film resistance (Rsf), and the medium frequency semicircle is related to the charge transfer (Rct) process.[55] The smaller the charge transfer resistance, the lower the potential polarization during charging. There is little difference between the surface facial mask impedance (Rf) and charge transfer resistance (Rct) values of PLLR and Mo 2% samples before cycling, but after 200 cycles, the difference between Rct values of PLLR and Mo 2% increases significantly after 200 cycles. The increase in Rf and Rct of PLLR can be attributed to the formation of additional SEI layers caused by side reactions during cycling.[55] Therefore, it is proved that the in situ generated heterostructure combined with the layered phase and rock salt can effectively avoid the transmission resistance caused by surface gaps, and the rock salt phase can effectively restrain the surface side reaction.

The GITT test results (Figure S6) show that the Mo 2% electrode is significantly higher than the PLLR electrode. The result is consistent with the previous charge–discharge test results. Moreover, the Mo doping can stabilize the lattice oxygen, limit anions to participation in redox, and inhibit irreversible O loss, resulting in a slight decrease in the D_{Li}^{+} value under high voltage compared with the PLLR. Therefore, it can be seen that the modification has a significant effect on stabilizing the crystal structure and improving the electrochemical performance.

In addition, TEM analysis is carried out on PLLR and Mo 2% samples after 200 cycles at 1 C, as shown in Figure 7. We can see three different regions from the inside to the outside of the PLLR samples after circulation, the typical layered lattice stripe *C*2/*m* phase, the intricate transition phase, and part of the rock salt phase (Figure 7a–d). It shows that the structure of PLLR produces a large number of phase transitions and serious particle breakage during the cycle process. The thickness of sites 1 and 2 is about 28–30 nm. However, Mo 2% samples still maintain the internal and external dual-phase structure (Figure 7e–g). Under the protection of the rock salt phase, the internal structure still maintains a very clear layered lattice stripe and a very complete particle. This further shows that the rock salt phase is helpful to reduce the phase transition during the cycle.

CONCLUSIONS

In summary, the heterostructure of the rock salt phase and layer phase can be induced by Mo doping. The induced rock salt phase is combined with the layered phase closely, such that the gap transmission resistance can be avoided, and the surface rock salt phase has a high reaction energy level with the electrolyte, which can effectively inhibit side reactions and phase transformation. In addition, the strong Mo–O bond energy can enhance lattice O and improve the structure

https://doi.org/10.1021/acsomega.2c07313
ACS Omega 2023, 8, 6720–6728

stability. The Mo 2% electrode shows an excellent cycle ability and rate performance, and the capacity retention rate is 79.7% after 300 cycles at 5 C. This strategy combines epitaxial heterostructure construction with strong TM−O bond formation, which can greatly improve the structural stability and provide a modification idea for layered oxides.

■ ASSOCIATED CONTENT

Supporting Information

The Supporting Information is available free of charge at https://pubs.acs.org/doi/10.1021/acsomega.2c07313.

EDS mapping diagrams of all elements in PLLR and Mo 2%. XRD Rietveld refinements and results for all samples. X-ray photoelectron spectroscopy (XPS) of O 1s in PLLR and Mo 2%. The element's concentration depth distribution based on XPS data. Mo 3d, Ni 2p, Mn 3s, and O 1s spectra for PLLR. Mo 3d, Ni 2p, Mn 3s, and O 1s spectra for Mo 2%. Quantification of the change of Mo concentration in Mo 2% with the depth of the particles by XPS. The discharge curves of the PLLR and Mo 2% sample at the 1st, 25th, 50th, 100th, and 200th cycle. The EIS diagram of the PLLR and Mo 2% samples. The Li^+ diffusion coefficient of the PLLR and Mo 2% electrodes before the cycle (PDF)

■ AUTHOR INFORMATION

Corresponding Author

Yang Song − *College of Chemical Engineering, Sichuan University, Chengdu 610065 Sichuan, China;* orcid.org/0000-0002-3754-7144; Email: songyang@scu.edu.cn

Authors

Yao Li − *College of Chemical Engineering, Sichuan University, Chengdu 610065 Sichuan, China*

Qing Zhao − *College of Chemical Engineering, Sichuan University, Chengdu 610065 Sichuan, China*

Mengke Zhang − *College of Chemical Engineering, Sichuan University, Chengdu 610065 Sichuan, China*

Lang Qiu − *College of Chemical Engineering, Sichuan University, Chengdu 610065 Sichuan, China*

Zhuo Zheng − *The State Key Laboratory of Polymer Materials Engineering, Polymer Research Institute of Sichuan University, Chengdu 610065 Sichuan, China*

Yang Liu − *School of Materials Science and Engineering, Henan Normal University, Xinxiang 453007 Henan, China*

Yan Sun − *School of Mechanical Engineering, Chengdu University, Chengdu 610106 Sichuan, China*

Benhe Zhong − *College of Chemical Engineering, Sichuan University, Chengdu 610065 Sichuan, China*

Xiaodong Guo − *College of Chemical Engineering, Sichuan University, Chengdu 610065 Sichuan, China;* orcid.org/0000-0003-0376-7760

Complete contact information is available at: https://pubs.acs.org/10.1021/acsomega.2c07313

Notes

The authors declare no competing financial interest.

■ ACKNOWLEDGMENTS

The authors kindly acknowledge the financial support from the National Natural Science Foundation of China (Grant Nos. U20A200201, 21878195, and 22108183), the Distinguished Young Scholars of Sichuan Province (2020JDJQ0027), 2020 Strategic cooperation project between Sichuan University and Zigong Municipal People's Government (No. 2020CDZG-09), 2020 Strategic cooperation project between Sichuan University and Luzhou Municipal People's Government (No. 2020CDLZ-20), State Key Laboratory of Polymer Materials Engineering (No. sklpme2020-3-02), Sichuan Provincial Department of Science and Technology (No. 2020YFG0471 and 2020YFG0022), Sichuan Province Science and Technology Achievement Transfer and Transformation Project (No. 21ZHSF0111), and Sichuan University's postdoctoral interdisciplinary Innovation Fund.

■ REFERENCES

(1) Liu, J.; Wang, J.; Ni, Y.; Zhang, K.; Cheng, F.; Chen, J. Recent breakthroughs and perspectives of high-energy layered oxide cathode materials for lithium-ion batteries. *Mater. Today* **2021**, *43*, 132−165.

(2) Li, W.; Erickson, E. M.; Manthiram, A. High-nickel layered oxide cathodes for lithium-based automotive batteries. *Nat. Energy* **2020**, *5*, 26−34.

(3) Ye, Z.; Zhang, B.; Chen, T.; Wu, Z.; Wang, D.; Xiang, W.; Sun, Y.; Liu, Y.; Liu, Y.; Zhang, J.; Song, Y.; Guo, X. A simple gas-solid treatment for surface modification of Li-rich oxides cathodes. *Angew. Chem., Int. Ed. Engl.* **2021**, *60*, 23248−23255.

(4) Choi, A.; Lim, J.; Kim, H.-J.; Jung, S. C.; Lim, H.-W.; Kim, H.; Kwon, M.-S.; Han, Y. K.; Oh, S. M.; Lee, K. T. Site-selective in situ electrochemical doping for Mn-rich layered oxide cathode materials in lithium-ion batteries. *Adv. Energy Mater.* **2018**, *8*, 1702514.

(5) Reddy, R. C. K.; Lin, X.; Zeb, A.; Su, C.-Y. Metal−organic frameworks and their derivatives as cathodes for Lithium-ion battery applications: A review. *Electrochem. Energy Rev.* **2022**, *5*, 312−347.

(6) Jiang, L.; Dong, D.; Lu, Y.-C. Design strategies for low temperature aqueous electrolytes. *Nano Res. Energy* **2022**, *1*, e9120003.

(7) Zhao, W.; Gao, L.; Ma, X.; Yue, L.; Zhao, D.; Li, Z.; Sun, S.; Luo, Y.; Liu, Q.; Asiri, A. M.; et al. An exquisite branch−leaf shaped metal sulfoselenide composite endowing an ultrastable sodium-storage lifespan over 10 000 cycles. *J. Mater. Chem. A* **2022**, *10*, 16962−16975.

(8) Zhao, W.; Wang, X.; Ma, X.; Yue, L.; Liu, Q.; Luo, Y.; Liu, Y.; Asiri, A. M.; Sun, X. In situ tailoring bimetallic−organic framework-derived yolk−shell NiS_2/CuS hollow microspheres: an extraordinary kinetically pseudocapacitive nanoreactor for an effective sodium-ion storage anode. *J. Mater. Chem. A* **2021**, *9*, 15807−15819.

(9) Liu, W.; Oh, P.; Liu, X.; Myeong, S.; Cho, W.; Cho, J. Countering voltage decay and capacity fading of lithium-rich cathode material at 60 °C by hybrid surface protection layers. *Adv. Energy Mater.* **2015**, *5*, 1500274.

(10) Wang, J.; He, X.; Paillard, E.; Laszczynski, N.; Li, J.; Passerini, S. Lithium- and manganese-rich oxide cathode materials for high-energy lithium-ion batteries. *Adv. Energy Mater.* **2016**, *6*, 1600906.

(11) Liu, J.; Hou, M.; Yi, J.; Guo, S.; Wang, C.; Xia, Y. Improving the electrochemical performance of layered lithium-rich transition-metal oxides by controlling the structural defects. *Energy Environ. Sci.* **2014**, *7*, 705−714.

(12) Wang, R.; He, X.; He, L.; Wang, F.; Xiao, R.; Gu, L.; Li, H.; Chen, L. Atomic structure of Li_2MnO_3 after partial de-lithiation and re-lithiation. *Adv. Energy Mater.* **2013**, *3*, 1358−1367.

(13) Zhao, E.; Li, Q.; Meng, F.; Liu, J.; Wang, J.; He, L.; Jiang, Z.; Zhang, Q.; Yu, X.; Gu, L.; Yang, W.; Li, H.; Wang, F.; Huang, X. Stabilizing the oxygen lattice and reversible oxygen redox chemistry through structural dimensionality in lithium-rich cathode oxides. *Angew. Chem., Int. Ed. Engl.* **2019**, *58*, 4323−4327.

(14) Xu, J.; Sun, M.; Qiao, R.; Renfrew, S. E.; Ma, L.; Wu, T.; Hwang, S.; Nordlund, D.; Su, D.; Amine, K.; Lu, J.; McCloskey, B. D.; Yang, W.; Tong, W.; et al. Elucidating anionic oxygen activity in lithium-rich layered oxides. *Nat. Commun.* **2018**, *9*, 947.

(15) Luo, K.; Roberts, M. R.; Hao, R.; Guerrini, N.; Pickup, D. M.; Liu, Y.-S.; Edstrom, K.; Guo, J.; Chadwick, A. V.; Duda, L. C.; Bruce, P. G. Charge-compensation in 3d-transition-metal-oxide intercalation cathodes through the generation of localized electron holes on oxygen. *Nat. Chem.* **2016**, *8*, 684−691.
(16) Hy, S.; Cheng, J.-H.; Liu, J.-Y.; Pan, C.-J.; Rick, J.; Lee, J.-F.; Chen, J.-M.; Hwang, B. J. Understanding the role of Ni in stabilizing the lithium-rich high-capacity cathode material Li-$[Ni_xLi_{(1-2x)/3}Mn_{(2-x)/3}]O_2$ $(0 \le x \le 0.5)$. *Chem. Mater.* **2014**, *26*, 6919−6927.
(17) Sathiya, M.; Abakumov, A. M.; Foix, D.; Rousse, G.; Ramesha, K.; Saubanere, M.; Doublet, M. L.; Vezin, H.; Laisa, C. P.; Prakash, A. S.; Gonbeau, D.; VanTendeloo, G.; Tarascon, J-M. Origin of voltage decay in high-capacity layered oxide electrodes. *Nat. Mater.* **2015**, *14*, 230−238.
(18) Hong, J.; Lim, H.-D.; Lee, M.; Kim, S.-W.; Kim, H.; Oh, S.-T.; Chung, G.-C.; Kang, K. Critical role of oxygen evolved from layered Li−excess metal oxides in lithium rechargeable batteries. *Chem. Mater.* **2012**, *24*, 2692−2697.
(19) Hy, S.; Felix, F.; Rick, J.; Su, W. N.; Hwang, B. J. Direct in situ observation of Li_2O evolution on Li-rich high-capacity cathode material, $Li[Ni_xLi_{(1-2x)/3}Mn_{(2-x)/3}]O_2$ $(0 \le x \le 0.5)$. *J. Am. Chem. Soc.* **2014**, *136*, 999−1007.
(20) Johnson, C. S.; Li, N.; Lefief, C.; Thackeray, M. M. Anomalous capacity and cycling stability of $xLi_2MnO_3\cdot(1-x)LiMO_2$ electrodes (M = Mn, Ni, Co) in lithium batteries at 50°C. *Electrochem. Commun.* **2007**, *9*, 787−795.
(21) Yabuuchi, N.; Yoshii, K.; Myung, S. T.; Nakai, I.; Komaba, S. Detailed studies of a high-capacity electrode material for rechargeable batteries, Li_2MnO_3-$LiCo_{1/3}Ni_{1/3}Mn_{1/3}O_2$. *J. Am. Chem. Soc.* **2011**, *133*, 4404−4419.
(22) Song, J.; Ning, F.; Zuo, Y.; Li, A.; Wang, H.; Zhang, K.; Yang, T.; Yang, Y.; Gao, C.; Xiao, W.; Jiang, Z.; Chen, T.; Feng, G.; Xia, D.; et al. Entropy stabilization strategy for enhancing the local structural adaptability of Li-rich cathode materials. *Adv. Mater.* **2022**, 2208726.
(23) Grimaud, A.; Hong, W. T.; Shao-Horn, Y.; Tarascon, J. M. Anionic redox processes for electrochemical devices. *Nat. Mater.* **2016**, *15*, 121−126.
(24) Li, Q.; Ning, D.; Wong, D.; An, K.; Tang, Y.; Zhou, D.; Schuck, G.; Chen, Z.; Zhang, N.; Liu, X. Improving the oxygen redox reversibility of Li-rich battery cathode materials via Coulombic repulsive interactions strategy. *Nat. Commun.* **2022**, *13*, 1123.
(25) Zhang, J.; Zhang, Q.; Wong, D.; Zhang, N.; Ren, G.; Gu, L.; Schulz, C.; He, L.; Yu, Y.; Liu, X. Addressing voltage decay in Li-rich cathodes by broadening the gap between metallic and anionic bands. *Nat. Commun.* **2021**, *12*, 3071.
(26) Dong, T.; Mu, P.; Zhang, S.; Zhang, H.; Liu, W.; Cui, G. How do polymer binders assist transition metal oxide cathodes to address the challenge of high-voltage lithium battery applications? *Electrochem. Energy Rev.* **2021**, *4*, 545−565.
(27) Liu, T.; Liu, J.; Li, L.; Yu, L.; Diao, J.; Zhou, T.; Li, S.; Dai, A.; Zhao, W.; Xu, S.; et al. Origin of structural degradation in Li-rich layered oxide cathode. *Nat.* **2022**, *606*, 305−312.
(28) Yu, H.; Cao, Y.; Chen, L.; Hu, Y.; Duan, X.; Dai, S.; Li, C.; Jiang, H. Surface enrichment and diffusion enabling gradient-doping and coating of Ni-rich cathode toward Li-ion batteries. *Nat. Commun.* **2021**, *12*, 4564.
(29) Liu, W.; Li, X.; Xiong, D.; Hao, Y.; Li, J.; Kou, H.; Yan, B.; Li, D.; Lu, S.; Koo, A.; Adair, K.; Sun, X. Significantly improving cycling performance of cathodes in lithium-ion batteries: The effect of Al_2O_3 and $LiAlO_2$ coatings on $LiNi_{0.6}Co_{0.2}Mn_{0.2}O_2$. *Nano Energy* **2018**, *44*, 111−120.
(30) Sun, Y. K.; Lee, M. J.; Yoon, C. S.; Hassoun, J.; Amine, K.; Scrosati, B. The role of AlF_3 coatings in improving electrochemical cycling of Li-enriched nickel-manganese oxide electrodes for Li-ion batteries. *Adv. Mater.* **2012**, *24*, 1192−1196.
(31) Wei, H.-x.; Huang, Y.-d.; Tang, L.-b.; Yan, C.; He, Z.-j.; Mao, J.; Dai, K.; Wu, X.-w.; Jiang, J.-b.; Zheng, J.-c. Lithium-rich manganese-based cathode materials with highly stable lattice and surface enabled by perovskite-type phase-compatible layer. *Nano Energy* **2021**, *88*, 106288.
(32) Xin, F.; Zhou, H.; Chen, X.; Zuba, M.; Chernova, N.; Zhou, G.; Whittingham, M. S. Li−Nb−O coating/substitution enhances the electrochemical performance of the $LiNi_{0.8}Mn_{0.1}Co_{0.1}O_2$ (NMC 811) cathode. *ACS Appl. Mater. Interfaces* **2019**, *11*, 34889−34894.
(33) Payandeh, S.; Strauss, F.; Mazilkin, A.; Kondrakov, A.; Brezesinski, T. Tailoring the $LiNbO_3$ coating of Ni-rich cathode materials for stable and high-performance all-solid-state batteries. *Nano Res. Energy* **2022**, *1*, e9120016.
(34) Li, Z.; Li, Y.; Zhang, M.; Yin, Z. W.; Yin, L.; Xu, S.; Zuo, C.; Qi, R.; Xue, H.; Hu, J.; et al. Modifying $Li@Mn_6$ superstructure units by Al substitution to enhance the long-cycle performance of Co-free Li-rich cathode. *Adv. Energy Mater.* **2021**, *11*, 2101962.
(35) Liu, Y.; Fan, X.; Zhang, Z.; Wu, H.-H.; Liu, D.; Dou, A.; Su, M.; Zhang, Q.; Chu, D. Enhanced electrochemical performance of Li-rich layered cathode materials by combined Cr doping and $LiAlO_2$ coating. *ACS Sustain. Chem. Eng.* **2019**, *7*, 2225−2235.
(36) Qing, R.-P.; Shi, J.-L.; Xiao, D.-D.; Zhang, X.-D.; Yin, Y.-X.; Zhai, Y.-B.; Gu, L.; Guo, Y.-G. Enhancing the kinetics of Li-rich cathode materials through the pinning effects of gradient surface Na^+ doping. *Adv. Energy Mater.* **2016**, *6*, 1501914.
(37) Zubair, M.; Li, G.; Wang, B.; Wang, L.; Yu, H. Electrochemical kinetics and cycle stability improvement with Nb doping for lithium-rich layered oxides. *ACS Appl. Energy Mater.* **2019**, *2*, 503−512.
(38) Nisar, U.; Muralidharan, N.; Essehli, R.; Amin, R.; Belharouak, I. Valuation of surface coatings in high-energy density lithium-ion battery cathode materials. *Energy Stor. Mater.* **2021**, *38*, 309−328.
(39) Yabuuchi, N.; Nakayama, M.; Takeuchi, M.; Komaba, S.; Hashimoto, Y.; Mukai, T.; Shiiba, H.; Sato, K.; Kobayashi, Y.; Nakao, A.; et al. Origin of stabilization and destabilization in solid-state redox reaction of oxide ions for lithium-ion batteries. *Nat. Commun.* **2016**, *7*, 13814.
(40) Kim, J.; Ma, H.; Cha, H.; Lee, H.; Sung, J.; Seo, M.; Oh, P.; Park, M.; Cho, J. A highly stabilized nickel-rich cathode material by nanoscale epitaxy control for high-energy lithium-ion batteries. *Energy Environ. Sci.* **2018**, *11*, 1449−1459.
(41) Xu, C.; Xiang, W.; Wu, Z.; Xu, Y.; Li, Y.; Wang, Y.; Xiao, Y.; Guo, X.; Zhong, B. Highly stabilized Ni-rich cathode material with Mo induced epitaxially grown nanostructured hybrid surface for high-performance lithium-ion batteries. *ACS Appl. Mater. Interfaces* **2019**, *11*, 16629−16638.
(42) Park, K.-J.; Jung, H.-G.; Kuo, L.-Y.; Kaghazchi, P.; Yoon, C. S.; Sun, Y.-K. Improved cycling stability of $Li[Ni_{0.90}Co_{0.05}Mn_{0.05}]O_2$ through microstructure modification by boron doping for Li-ion batteries. *Adv. Energy Mater.* **2018**, *8*, No. 1801202.
(43) Liao, Y.; Li, J.; Deng, B.; Wang, H.; Chen, T.; Li, X.; Qu, M.; Li, X.; Peng, G. Surface modification of $Li_{1.144}Ni_{0.136}Co_{0.136}Mn_{0.544}O_2$ by hybrid protection layer with enhanced rate capability. *Energy Technol.* **2020**, *8*, 1901133.
(44) Wu, Z.; Ji, S.; Liu, T.; Duan, Y.; Xiao, S.; Lin, Y.; Xu, K.; Pan, F. Aligned Li^+ tunnels in core-shell $Li(Ni_xMn_yCo_z)O_2@LiFePO_4$ enhances its high voltage cycling stability as Li-ion battery cathode. *Nano Lett.* **2016**, *16*, 6357−6363.
(45) Wang, Y.; Yang, Z.; Qian, Y.; Gu, L.; Zhou, H. New insights into improving rate performance of lithium-rich cathode material. *Adv. Mater.* **2015**, *27*, 3915−3920.
(46) Yi, T.-F.; Chen, B.; Zhu, Y.-R.; Li, X.-Y.; Zhu, R.-S. Enhanced rate performance of molybdenum-doped spinel $LiNi_{0.5}Mn_{1.5}O_4$ cathode materials for lithium-ion battery. *J. Power Sources* **2014**, *247*, 778−785.
(47) Li, S.; Fu, X.; Liang, Y.; Wang, S.; Zhou, X. a.; Dong, H.; Tuo, K.; Gao, C.; Cui, X. Enhanced structural stability of boron-doped layered@spinel@carbon heterostructured lithium-rich manganese-based cathode materials. *ACS Sustain. Chem. Eng.* **2020**, *8*, 9311−9324.
(48) Yu, Z.; Shang, S.-L.; Gordin, M. L.; Mousharraf, A.; Liu, Z.-K.; Wang, D. Ti-substituted $Li[Li_{0.26}Mn_{0.6-x}Ti_xNi_{0.07}Co_{0.07}]O_2$ layered

https://doi.org/10.1021/acsomega.2c07313
ACS Omega 2023, 8, 6720−6728

cathode material with improved structural stability and suppressed voltage fading. *J. Mater. Chem. A* **2015**, *3*, 17376−17384.
(49) Cho, Y.; Oh, P.; Cho, J. A new type of protective surface layer for high-capacity Ni-based cathode materials: nanoscaled surface pillaring layer. *Nano Lett.* **2013**, *13*, 1145−1152.
(50) Li, Q.; Ning, D.; Zhou, D.; An, K.; Wong, D.; Zhang, L.; Chen, Z.; Schuck, G.; Schulz, C.; Xu, Z.; et al. The effect of oxygen vacancy and spinel phase integration on both anionic and cationic redox in Li-rich cathode materials. *J. Mater. Chem. A* **2020**, *8*, 7733−7745.
(51) Yu, Y.; Yang, Z.; Zhong, J.; Liu, Y.; Li, J.; Wang, X.; Kang, F. A simple dual-ion doping method for stabilizing Li-rich materials and suppressing voltage decay. *ACS Appl. Mater. Interfaces* **2020**, *12*, 13996−14004.
(52) Ting, M.; Burigana, M.; Zhang, L.; Finfrock, Y. Z.; Trabesinger, S.; Jonderian, A.; McCalla, E. Impact of nickel substitution into model Li-rich oxide cathode materials for Li-ion batteries. *Chem. Mater.* **2020**, *32*, 849−857.
(53) Lee, Y.; Shin, J.; Kang, H.; Lee, D.; Kim, T. H.; Kwon, Y. K.; Cho, E. Promoting the reversible oxygen redox reaction of Li-excess layered cathode materials with surface vanadium cation doping. *Adv. Sci.* **2021**, *8*, 2003013.
(54) Cao, X.; Qiao, Y.; Jia, M.; He, P.; Zhou, H. Ion-Exchange: A promising strategy to design Li-rich and Li-excess layered cathode materials for Li-ion batteries. *Adv. Energy Mater.* **2022**, *12*, 2003972.
(55) Li, Q.; Li, G.; Fu, C.; Luo, D.; Fan, J.; Li, L. K^+-doped $Li_{1.2}Mn_{0.54}Co_{0.13}Ni_{0.13}O_2$: a novel cathode material with an enhanced cycling stability for lithium-ion batteries. *ACS Appl. Mater. Interfaces* **2014**, *6*, 10330−10341.

https://doi.org/10.1021/acsomega.2c07313
ACS Omega 2023, 8, 6720−6728